The Center for Particle Theory

THE UNIVERSITY OF TEXAS AT AUSTIN

SHOCK WAVES IN RELATIVISTIC NUCLEAR MATTER, I

A. M. Gleeson and S. Raha

Center for Particle Theory
Department of Physics
University of Texas at Austin
Austin, Texas 78712

Abstract

We develop the relativistic Rankine-Hugoniot relations for a 3-dimensional plane shock and a 3-dimensional oblique shock. Using these discontinuity relations together with various equations of state for nuclear matter, we calculate the temperatures and the compressibilities attainable by shock compression for a wide range of laboratory kinetic energy of the projectile.

Introduction

During the past few years, accelerators have been developed which are capable of producing reasonably intense beams of energetic nuclei. These heavy ion accelerators are now producing beams with projectile energies in the range of 200-800 Mev/nulceon. Continued development of these machines will produce more energetic and larger nuclei projectile beams. Development of the analysis of these experiments will require a comprehensive knowledge of a model of nuclear matter which is consistent with our current ideas of the nuclear fluid and is capable of extension to the domain of these relativistic energies. In fact, even at the current levels of machine operations, the correction to nonrelativistic treatments are becoming manifest. The energies per nucleon require an approximate 10% correction to account for the relativistic kinematics. They allow the production of low mass mesons and collective effects in nuclear matter propagate at speeds comparable to the speed of light.

Recently a model of nuclear matter which is fully relativistic and which reproduces the essential features of nuclear matter at nuclear density has been developed.[1] This model has the added feature that it is extendable to include finite temperature effects in the nuclear fluid.

In this paper, we will use this model and others to investigate the hydrodynamics of heavy ion collisions. The purpose of this study is to examine the range of temperatures

and compressibilities attainable in heavy ion collisions and to determine the order of magnitude of the correction due to the relativistic kinematics and interactions. The specific phenomenon which we treat here is the heating due to shock wave formation. The choice of this process is based on the realization that shock heating is one of the most effective mechanisms for the conversion of kinetic energy to heat energy in ideal fluids. In the next section of this paper, we review the properties of the model of nuclear matter which is the basis of this study. In section III, we extend the nonrelativistic treatment of shock formation in nuclear matter, to the relativistic domain. We ther combine these results to examine the ranges of temperature expected in heavy ion collisions. In the final section of this paper, we present several possible implications of these results.

II. The Equations of State

Throughout this paper, four equations of state for the nuclear fluid will be utilized. Two of these are the non-interacting Fermi gas in the relativistic and nonrelativistic kinematics. The third case, used mostly for analytic results, is the relativistic polytrope. These cases are well enough known not to warrant any review here. The fourth equation of state used for the nuclear fluid is an interesting relativistic model developed earlier.[1] Here we present a review of its essential inputs and result. All these models are solvable in the finite temperature limit.[2]

The fundamental interactions for the interacting case are the phenomenological four Fermi interaction with scalar and vector couplings. The effective Lagrangian for nuclear matter is

$$L = L_0 - \sum_{B=p,n} \lambda_s^2 \bar{\psi}_B(x)\psi_B(x)\bar{\psi}_B(x)\psi_B(x)$$

$$+ \sum_{B=p,n} \lambda_v^2 \bar{\psi}_B(x)\gamma^\mu\psi_B(x)\bar{\psi}_B(x)\gamma_\mu\psi_B(x) \qquad (1)$$

where L_0 is the usual free Fermion Lagrangian. It can be solved in the finite temperature self-consistent Hartree approximation. The coupling constants λ_s and λ_v are fixed by matching the properties of nuclear matter at T = 0. This fit gives,

$$\frac{\lambda_s^2 m^2}{\pi^2} = 27.04 \ , \qquad \frac{\lambda_v^2 m^2}{\pi^2} = 19.83 \ , \qquad (2)$$

where m is the nucleon mass. Besides fitting nuclear matter, these values are found to yield very good scattering amplitude in agreement with the low energy nucleon nucleon scattering data.[3] The stress energy tensor generated by this Lagrangian takes the form of a perfect fluid and all thermodynamic variables are thence derivable. The results of these calculations are an interacting fluid with the equations of state summarized in figures 2.1, 2.2, 2.3 and 2.4. The fluid displays a broad phase transition with behavior that differs markedly from that of a free gas for densities near the nuclear density and at low temperatures. For comparison, a model based on a noninteracting relativistic fluid (figures 2.5, 2.6 and 2.7), a non-interacting nonrelativistic Fermi fluid (figures 2.8 and 2.9), and a nonrelativistic non-interacting Boltzmann fluid (figure 2.10) are also included.

III. Shock Waves in Nuclear Matter

The analysis of shock formation in very dense or super-dense matter requires the joining of relativistic kinematics to the well-known discontinuity conditions of strong shock waves. We treat the cases: (a) the formation of plane normal shock waves and (b) the oblique shocks. These two limits are of interest since they correspond to the cases of a large nucleus-large nucleus collision and to small projectile-large nucleus collision, respectively.

As stated earlier, the stress energy tensor is that of a perfect fluid and takes the form

$$T^{\mu\nu} = pg^{\mu\nu} + (p+\rho)u^{\mu}u^{\nu} \ , \tag{3}$$

where p and ρ are the pressure and the energy density and u^{μ} is the four velocity of the fluid. The baryon number current density is

$$j^{\mu} = n_0 u^{\mu} \ , \tag{4}$$

where n_0 is the baryon number density. The relativistic shock discontinuity equations follow from the laws of conservation of energy momentum and baryon number.[4] These are

$$\partial_{\mu} T^{\mu\nu} = 0 \tag{5}$$

$$\partial_{\mu} j^{\mu} = 0 \tag{6}$$

Case (a): Plane Shock

For plane wave shocks, equations (3)-(6) can be evaluated for plane wave geometry across a volume containing the shock front. These yield

$$(p_+ + \rho_+)u_+^z u_+^0 = (p_- + \rho_-)u_-^z u_-^0 \tag{7}$$

$$(p_+ + \rho_+)u_+^z u_+^x = (p_- + \rho_-)u_-^z u_-^x \tag{8}$$

$$(p_+ + \rho_+)u_+^z u_+^y = (p_- + \rho_-)u_-^z u_-^y \tag{9}$$

$$p_+ g^{ZZ} + (p_+ + \rho_+)u_+^z u_+^z = p_- g^{ZZ} + (p_- + \rho_-)u_-^z u_-^z \tag{10}$$

$$n_{0+}u_+^z = n_{0-}u_-^z \tag{11}$$

where the co-ordinate system is such that the shock front is in the xy plane and is located at $z = 0$. The subscript (+) denotes the variables evaluated in the region $z > 0$ and (-) designates the region $z < 0$. Equations (7), (8) and (9) yield

$$\frac{u_+^x}{u_+^0} \equiv v_+^x = v_-^x \equiv \frac{u_-^x}{u_-^0} \tag{12}$$

and

$$\frac{u_+^y}{u_+^0} \equiv v_+^y = v_-^y \equiv \frac{u_-^y}{u_-^0} \tag{13}$$

This is the same condition which emerges nonrelativistically.[5] There is no change in the velocity components parallel to the plane of the shock front. For the case of normal shock we chose a Lorentz frame where $v_+^x = v_-^x = v_+^y = v_-^y = 0$. Equation (10) can be written as

$$p_+ + (p_+ + \rho_+)u_+^z u_+^z = p_- + (p_- + \rho_-)u_-^z u_-^z \qquad (14)$$

These are the Rankine-Hugoniot relations for a relativistic plane shock phenomenon. By inspection of the R-H relations, we can immediately conclude that this is a deterministic system once we include the equation of state for the shocked fluid. For later convenience, we rewrite the R-H relations in the rest frame of the shocked fluid by means of a Lorentz transformation. The advantage of this lies in the realization that this is also the CM frame for a central collision of two equal heavy ions. Equations (12) and (13) then allow us to reduce the problem to one-dimensional hydrodynamics. At this point, we also make the assumption that before the collision, the nuclear matter is cold and in its ground state so that we can assume that p_- is small in comparison with p_+.

Then equations (7), (10), and (11) may be equivalently rewritten as

$$p_+ = \rho_-(v_0' + v_s)\gamma_0'^2 v_0' \qquad (15a)$$

$$\rho_+ v_s = \rho_-(v_0' + v_s)\gamma_0'^2 \qquad (15b)$$

$$n_{0+} v_s = n_{0-}(v_0' + v_s)\gamma_0' \qquad (15c)$$

where v_0' is the 3-velocity of the incoming (unshocked) fluid as measured in the rest frame of the shocked fluid, v_s is the 3-velocity of the shock front as measured in the rest frame of the shocked fluid and $\gamma_0' = (1 - v_0'^2)^{-1/2}$ is the usual Lorentz factor.

We also introduce the concept of specific internal energy as

$$E_{\pm} = \frac{\rho_{\pm}}{n_{0\pm}}$$

and the compression ratio

$$\nu = \frac{n_{0+}}{n_{0-}} \quad .$$

Then with the help of these definitions together with equations (15), we get

$$E_+ = E_-\gamma_0' \tag{16}$$

$$p_+ = E_-n_{0+}\frac{(\gamma_0'^2 - 1)}{(\nu - \gamma_0')} \tag{17}$$

$$v_s = \frac{v_0'\gamma_0'}{\nu-\gamma_0'} \tag{18}$$

These equations are the relativistic extension of the shock discontinuity equations of Sobel et al.[6]

They are the basis of our analysis of relativistic plane wave shocks in nuclear matter.

Although not markedly different in appearance than their nonrelativistic counterparts, the implications of these equations are very different. For a polytropic equation of state,

$$\rho = n_0 m + \frac{p}{\beta - 1} \quad ,$$

where β is the polytropic index.

then the compression ratio is

$$\nu = \gamma_0' \left(\frac{\gamma_0'(v_0')^2 + (\beta-1)(\gamma_0'-1)}{(\beta-1)(\gamma_0'-1)} \right) \quad .$$

For small v_0' this reduces to the usual nonrelativistic result that

$$\nu = \frac{\beta + 1}{\beta - 1} \quad , \tag{19}$$

which implies that the compression ratio is bounded. For a nonrelativistic gas at high temperatures β is 5/3. This bounds the

compression ratio at 4. In the relativistic limit for this same case

$$\nu = \gamma_0' \frac{\beta}{\beta - 1} .$$

Here the compression ratio is unbounded. If instead of the proper densities a new compression ratio, using the densities as measured in the rest frame of the shocked fluid is defined, then

$$\nu' = \frac{\beta}{\beta - 1} .$$

This compression ratio is bounded and for the same case as above, except that now the appropriate polytropic index is 4/3, yields a ν' of 4.

For comparison with the interacting and relativistic case we derive the nonrelativistic internal energy change for a free Boltzmann gas. We have then

$$E_+ - E_- = \left(\frac{\nu - 1}{\nu}\right) \frac{1}{2n_{0-}} p_+$$
$$= \frac{3T_+}{2}$$

for a noninteracting gas with equation of state $p = nT$. This result is plotted in Figure 4.1.

However, for a realistic equation of state, the adiabatic

index is not constant across the shock front and one must solve for the compression ratio numerically as a function of incoming velocity of the unshocked fluid. Details of these calculations are presented in section IV.

Case (b): Oblique Shock

In this section, we analyze the shock formed by the collision of a small projectile (approximated by a point particle) with a large nucleus at rest which we will treat as a semi-infinite slab of fluid. As is well known, the disturbance will be confined within a cone whose opening angle is determined by the velocity of the supersonic projectile and also the sound velocity in the fluid.[5] Let us define the z-direction parallel to the velocity of the projectile. We chose to work in cylindrical co-ordinates.

Then the baryon number density current as a function of space and time variables in the frame of shock is (figure 3.1)

$$j^{\mu}(\rho,\phi,z,t)$$

$$= \theta(z)\theta(-\rho + z\tan\theta)n_{0+}u_{+}^{\mu}$$

$$+ \theta(z)\theta(\rho - z\tan\theta)n_{0-}u_{-}^{\mu}$$

$$+ \theta(-z)n_{0-}u_{-}^{\mu} \quad , \qquad (20)$$

where $\theta(x)$ is the usual step function. Continuity of baryon number flux across the shock front is given by

$$\int_{V_4 \supset \text{shock}} \partial_\mu j^\mu d^4x = 0 \tag{21}$$

We look at a thin slab specified by $t_2 \leq t \leq t_1$, $-\infty < z \leq \delta(\tan\theta)^{-1}$, $-\varepsilon < \rho - z\tan\theta < \varepsilon$ and $0 < \phi \leq 2\pi$.

Then we must have

$$2\pi(t_2-t_1)\iint \rho d\rho dz \partial_\mu j^\mu = 0 \ .$$

$$\partial_\mu j^\mu = \frac{\partial j^z}{\partial z} + \frac{\partial j^\rho}{\partial \rho} + \rho\frac{\partial j^\phi}{\partial \phi}$$

$$= \delta(z) j^z (\theta(\rho - z\tan\theta) - 1)$$

$$+ \theta(z)\delta(\rho - z\tan\theta)[j_+^z - j_-^z]\tan\theta$$

$$+ \delta(z)\theta(-\rho + z\tan\theta) j_+^z$$

$$- \theta(z)\delta(\rho - z\tan\theta)(j_+^\rho - j_-^\rho) \ .$$

Evaluating the integrals, we get,

$$j_+^z \tan\theta - j_+^\rho = j_-^z \tan\theta - j_-^\rho \quad ,$$

or
$$n_{0+}[u_+^z \tan\theta - u_+^\rho] = n_{0-}[u_-^z \tan\theta - u_-^\rho] \tag{21}$$

Energy momentum conservation is given by

$$\int d^4x \partial_\mu T^{\mu\nu} = 0 \quad , \tag{22}$$

which can equivalently be written as, via Stokes' theorem,[4]

$$[T^{\mu\nu}]_{n_\nu} = 0 \tag{23}$$

where [ ] means taking the difference between the corresponding quantities across the surface of discontinuity and n_ν is the unit normal vector to the hypersurface.

Here

$$\hat{n} = \hat{z}\sin\theta - \hat{\rho}\cos\theta \quad . \tag{24}$$

We then have the following relations:

$$(p_+ + \rho_+)u_+^0(u_+^z\sin\theta - u_+^\rho\cos\theta)$$

$$= (p_- + \rho_-)u_-^0(u_-^z\sin\theta - u_-^\rho\cos\theta) \qquad (25)$$

$$p_+\cos\theta - (p_+ + \rho_+)u_+^\rho(u_+^z\sin\theta - u_+^\rho\cos\theta)$$

$$= p_-\cos\theta - (p_- + \rho_-)u_-^\rho(u_-^z\sin\theta - u_-^\rho\cos\theta) \qquad (26)$$

$$p_+\sin\theta + (p_+ + \rho_+)u_+^z(u_+^z\sin\theta - u_+^\rho\cos\theta)$$

$$= p_-\sin\theta + (p_- + \rho_-)u_-^z(u_-^z\sin\theta - u_-^\rho\cos\theta) \qquad (27)$$

$$(p_+ + \rho_+)u_+^\phi(u_+^z\sin\theta - u_+^\rho\cos\theta)$$

$$= (p_- + \rho_-)u_-^\phi(u_-^z\sin\theta - u_-^\rho\cos\theta) \qquad (28)$$

From (28) and (25), we get

$$\frac{u_+^\phi}{u_+^0} \equiv v_+^\phi = v_-^\phi \equiv \frac{u_-^\phi}{u_-^0} \qquad (29)$$

(26) and (27) can be manipulated to yield

$$p_+ + (p_+ + \rho_+)(u_+^z \sin\theta - u_+^\rho \cos\theta)^2$$

$$= p_- + (p_- + \rho_-)(u_-^z \sin\theta - u_-^\rho \cos\theta)^2 \qquad (30)$$

and

$$(p_+ + \rho_+)(u_+^z \sin\theta - u_+^\rho \cos\theta)(u_+^z \cos\theta + u_+^\rho \sin\theta)$$

$$= (p_- + \rho_-)(u_-^z \sin\theta - u_-^\rho \cos\theta)(u_-^z \cos\theta + u_-^\rho \sin\theta) \qquad (31)$$

Then (25) and (31) yield

$$\frac{(u_+^z \cos\theta + u_+^\rho \sin\theta)}{u_+^0} = \frac{u_-^z \cos\theta + u_-^\rho \sin\theta}{u_-^0}$$

or

$$v_+^z \cos\theta + v_+^\rho \sin\theta = v_-^z \cos\theta + v_-^\rho \sin\theta \qquad (32)$$

Equation (30) is the usual continuity of momentum flux normal to the surface of discontinuity. Equation (32) is the same as obtained for the continuity of tangential velocity for oblique shock in the nonrelativistic case. By the suitable choice of our z-direction, we have set $v_-^\rho = v_-^\phi = 0$ which, by (29), implies $v_+^\phi = 0$, but v_+^ρ has a nonzero value. As in the nonrelativistic case, the fluid velocity, after passing through the oblique shock, inclines toward the shock front. Using the same approximation as before ($p_- \approx 0$, compared to p_+), we can considerably simplify the problem.

We have 4 discontinuity equations together with the equation of state for shocked matter. The number of unknown parameters, including the opening angle of the shock front is now 6. Thus the system is indeterminant. As is the case with nonrelativistic oblique shocks, we can reduce this indeterminancy to a single function called the shock polar. Figure 4.2 is a schematic example of shock polar. Figures 4.3 are actually calculated shock polars.

The shock polar is used to analyze the shock wedge as shown in fig. 4.2. For matter scattered off the point projectile through a deviation angle of χ, the flow behind the shock is at point P in the figure. The opening angle of the shock wedge is the angle θ of the line perpendicular to the cord PQ of the shock polar. For each χ, there are two shock states P' and P which correspond to the motion behind shock being subsonic and supersonic, respectively, and clearly, they correspond to different opening angles. The extremal deviation angle χ_{ext} (for point P_{ext}) corresponds to the transition point between these regimes. The corresponding opening angle is θ_{ext}. The angle α in the figure gives the mach angle, which is the opening angle for a very weak shock.

In the case of a nonrelativistic polytrope, the analytical form of the shock polar is well known.[5,7] For the relativistic polytrope, we can perform a similar analysis.

We have

$$p_+ = n_{0+}[E_+ - E_-](\beta-1) \ . \qquad (32)$$

Using this with equations (21)-(31) and after some straightforward transformations, we obtain

$$\nu \equiv \frac{n_{0+}}{n_{0-}} = \frac{\beta + \alpha}{\beta - 1} \qquad \text{where } \alpha \equiv \frac{u_-^0}{u_+^0} \quad . \tag{33}$$

In the nonrelativistic limit, $\alpha \to 1$, and we obtain our previous result for ν.

Using (33) in (21) and (31), we obtain

$$(v_+^\rho)^2 = (v_-)^2 \frac{(1-\beta)\alpha}{\beta + \alpha} + (v_+^z v_-) \frac{\beta(\alpha+1)}{\beta + \alpha} - (v_+^z)^2 \quad . \tag{34}$$

This is the equation of the shock polar. Again, in the nonrelativistic limit, it reduces to the appropriate familiar form

$$(v_+^\rho)^2 = (v_- - v_+^z) \cdot \left[v_- \left(\frac{1 - \beta}{\beta + 1} \right) + v_+^z \right] \quad . \tag{35}$$

From equation (34), one can readily calculate the maximum value of the angle of deviation. χ_{max} is given by

$$\chi_{max} = \tan^{-1} \left\{ \left(\frac{\beta^2(\alpha+1)^2 - 2\beta^2(\alpha+1)^2\alpha - 4\alpha(1-\beta)(\beta+\alpha)}{4(1-\beta)(\beta+\alpha)\alpha} \right)^{1/2} \right\}$$

which, as expected, reduces to the familiar nonrelativistic result

$$\chi_{max} = \tan^{-1} \left(\frac{1}{\sqrt{\beta^2 - 1}} \right) \quad .$$

In the nonrelativistic case, one can analytically find the corresponding opening angle θ which is given by

$$\sin^2\theta = \frac{\beta + 1}{2\beta} \quad . \tag{36}$$

It is obvious from the above discussion that the extremal angle of deviation in the relativistic case depends on the velocity of the fluid through the occurrence of α in the expression for χ_{max}. However, in the nonrelativistic case, χ_{max} does not depend on any velocity at all. An inspection of figures 4.3 verifies this observation.

For a nonrelativistic polytrope with equation of state $P = n_0 T$ and polytropic index β, we have the following Rankine-Hugoniot relations for a strong shock, with $v_- = v_-^z \hat{z}$.

$$n_{0+}(v_+^z \sin\theta - v_+^\rho \cos\theta) = n_{0-}(v_-^z \sin\theta) \tag{37a}$$

$$\left(\frac{\beta}{\beta-1}\right)\frac{T_+}{m} + \frac{1}{2}(v_+^z \sin\theta - v_+^\rho \cos\theta)^2 = \frac{1}{2}(v_-^z \sin\theta)^2 \tag{37b}$$

$$n_{0+}\frac{T_+}{m} + n_{0+}(v_+^z \sin\theta - v_+^\rho \cos\theta)^2 = n_{0-}(v_-^z \sin\theta)^2 \tag{37c}$$

$$v_+^z \cos\theta + v_+^\rho \sin\theta = v_-^z \cos\theta \quad . \tag{37d}$$

(37a,b,c) together yield (19)

From (19), (37a) and (37b), we derive

$$\frac{T_+}{m} = 2(v_-^z)^2 \frac{\sin^2\theta(\beta-1)}{(\beta+1)^2}$$

$$\text{or,} \quad T_+ = \frac{1}{2}m(v_-^z)^2 \frac{4\sin^2\theta(\beta-1)}{(\beta+1)^2}$$

$$= \frac{2(\beta-1)}{\beta(\beta+1)} E_{Lab} \quad . \tag{38}$$

where we have used (36).

Then for a certain β, we can immediately calculate T_+ for any E_{Lab}. Results for $\beta = 5/3$ are in figure 4.4. These are the temperatures corresponding to χ_{ext}.

However, for a realistic equation of state, one must take recourse to a numerical analysis involving the Rankine-Hugoniot relations and the equation of state to obtain the shock polar. Details of the analysis are given in the following section.

IV. Numerical Results

As explained in the previous section, the Rankine-Hugoniot relations together with the equation of state of the nuclear fluid make the system deterministic for the normal shock and reduce to a single free parameter for the oblique or mach cone shock. We calculate the temperature generated by the shock compression for both kinds of collisions for the four equations of state of interest (a nonrelativistic noninteracting gas, a relativistic noninteracting gas and a realistic, relativistic strongly interacting gas). The analysis is particularly simple and analytical for a nonrelativistic noninteracting gas and a relativistic polytrope for both shock geometries (see previous section). In other cases, one has to take recourse to numerical iterations which, however, are not very complicated.

Case (a): Plane Wave Shock

For a relativistic noninteracting gas and also for a relativistic strongly interacting gas, we solve for the temperature through an iterative procedure. Knowing the CM velocity corresponding to a certain lab energy of the projectile, and under the assumption of zero initial temperature and pressure, one immediately knows the specific internal energy behind the shock front, by equation (16). From the equation of state, one can calculate the number densities and the corresponding temperatures which answer to that specific energy. At this point, it must be noted that as opposed to the nonrelativistic case, the relativistic specific internal energy includes the

mass of a baryon. For each of the temperatures and the number densitie one can calculate the pressure from Rankine-Hugoniot relatio (tion 17) and also from the equation of state. The tem ure and the number density for which these two pressures agree is to be accepted as the correct number density and the correct temperature in the shock compressed matter corresponding to that particular lab energy of the projectile. This process is repeated for a wide range of lab energies and the results are summarized in figure 4.1 (curve a for relativistic noninteracting Fermi gas and curve c for relativistic interacting Fermi gas).

Case (b): Oblique Shock

The nonrelativistic noninteracting polytrope, has already been discussed in the previous section. One obtains a linear relationship between the temperature and the lab kinetic energy of the projectile. Results with $\beta = 5/3$ are shown in figure 4.4 (curve a).

For relativistic equations of state (both interacting and noninteracting), the following numerical iteration procedure is used. For a specific lab energy of the projectile (taken to be a point particle), one can find a speed v_+ for which a set of values of p_+, n_{0+}, ρ_+ satisfy the relation

$$\left(\frac{p_+ + \rho_+}{n_{0+}}\right) u_+^0 = \left(\frac{p_- + \rho_-}{n_{0-}}\right) u_-^0 \qquad (39)$$

obtained from equations (21) and (25). By a suitable choice of the z-axis, we set $v_-^\rho = v_-^\phi = 0$. We also impose the condition $|\vec{v}_+| \leq |\vec{v}_-|$ to eliminate spurious solutions. Then under the strong shock approximation, θ can be eliminated from equations (21) and (32) to obtain

$$v_+^z = (n_{0-}v_-^2u_-^0 + n_{0+}v_+^2u_+^0)/(n_{0-}u_-^0 + n_{0+}u_+^0)v_- \quad . \qquad (40)$$

So for each value of n_{0+} (and the associated p_+ and ρ_+) for which $|\vec{v}_+| \leq |\vec{v}_-|$, one can calculate v_+^z from equation (40) and consequently v_+^ρ from the following relation

$$v_+^2 = (v_+^z)^2 + (v_+^\rho)^2 + (v_+^\phi)^2$$

$$= (v_+^z)^2 + (v_+^\rho)^2 \quad . \qquad (41)$$

θ can also be eliminated from (21) and (26) to yield

$$\frac{p_+ n_{0+} u_+^z}{p_+ + (p_+ + \rho_+)(u_+^\rho)^2} = n_{0-}u_-^z \quad . \qquad (42)$$

If u_+^z and u_+^ρ calculated from (40) and (41) satisfy equation (42) for the corresponding p_+ and ρ_+, they belong to the

shock polar. These values of v_+^z and v_+^ρ are plotted for different equations of state for different lab energies of the projectile in figures 4.3. In each of these polar graphs, P denotes the point where the two shock configurations coincide. For that particular point, we immediately know what number density, energy density and pressure exist in the shocked matter and consequently we know the corresponding temperature from the equation of state. Temperature versus lab kinetic energies for point P on the shock polar are given in figure 4.4

V. Discussions

Inspection of the results (figs. 4.1 and 4.4) imply that the temperatures generated by the shock compression are affected by the equation of state and the relativistic kinematics. These effects distribute themselves with energy as expected. Figure 4.1 indicates that the interactions play a very significant role at energies in which shock heating is initiated. There are also large effects associated with species and the heating mechanism. Comparison of curve a in fig. 4.1 with b and e distinguishes the case of shock heating from the unrealistic but commonly used cases of heating by turning all the kinetic energy into internal energy. Curves b and e and curves f and d show the effect of species change. Comparison of curves a and c in fig. 4.1 shows the distinction between interacting and noninteracting cases of the same species. Curve d is the extreme example of a nonrelativistic Boltzmann gas heated by internal energy conversion under nonrelativistic kinematics. Comparison of a and f shows the distinction due to kinematics.

For the relativistic interacting Fermi gas, the effect of vector repulsion is dominant in the range of interest (number density from $10^{38}/cm^3$ to $10^{39}/cm^3$) and consequently, it is harder than the noninteracting gas of the same species under the same kinematics. As a result, the interacting gas is less compressible and comparatively more energy can be thermalized,

yielding a higher temperature than in the noninteracting case. This is depicted by the curves c and a in fig. 4.1. Because of the softness of the noninteracting gas, there is no appreciable rise in temperature until the lab kinetic energy is high enough to first compress the matter sufficiently (as required by the Rankine-Hugoniot conditions) and still have left enough energy to be thermalized afterwards.

Calculated temperatures from the interacting equations of state are in excellent qualitative agreement with the earlier estimates of Chapline et al.[8] Recently, Chin[9] has used an almost equivalent equation of state to estimate the temperatures of heavy ion collisions for different values of the compression ratio. Our calculations agree qualitatively with his estimates with the exception that we observe no such necessity to consider an arbitrary range of compression ratios, the process (in the plane shock) being fully determined by the Rankine-Hugoniot relations and the equation of state.

In free Boltzmann gas, both relativistic and nonrelativistic (curves b and d in fig. 4.1), the specific internal energy is a function of temperature only. Therefore when one estimates the temperature by assuming that all the kinetic energy is converted to internal energy, no compressional energy is accounted for and consequently one obtains higher temperatures. Clearly, these are unrealistic models. For completeness, in curve d, we have nonrelativistic kinematics. This

case is unphysical since the speed of matter is greater than the speed of light. For the same reason, curve f is also unphysical.

For a relativistic free Fermi gas (curve e), the specific internal energy depends on both temperature and the number density due to Fermi degeneracy. Therefore, we estimate the temperatures, assuming that the number density in shocked matter is just twice the density (corrected by the appropriate Lorentz factor). This corresponding temperature is higher than the Rankine-Hugoniot case (curve a) but the number density violates the softness requirement of the equation of state and is therefore not physical.

For the collision of a single baryon projectile with a heavy ion (figs. 4.3 (i,ii,iii) and 4.4), we observe the same qualitative nature. Inspection of curves (a) and (b) in figs. 4.3 (i,ii,iii) indicates the dependence of the shock polar on the equation of state. In all three lab energies shown here, the maximum angle of deviation χ_{max} is greater for the noninteracting Fermi gas than for the interacting Fermi gas. This is shown by explicit construction in fig. 4.3 (ii). In fig. 4.3 (ii), we also notice that angle 3 (mach angle for free gas) is smaller than angle 4 (mach angle for interacting gas) as the speed of sound in cold fluid for the interacting case is higher.

In our analysis of the nonrelativistic polytrope in

section III(b), we found that χ_{max} is given by

$$\chi_{max} = \tan^{-1}\left(\frac{1}{\sqrt{\beta^2 - 1}}\right) = \sin^{-1}(1/\beta) \ .$$

Harder equation of state corresponds to higher β and consequently lower values of χ_{max}. This same trend is also prevalent in relativistic kinematics.

The effect of kinematics on the shock polar is obvious from the differences in curves a and c in figs. 4.3 (i and ii). That curve c presents a completely unphysical configuration is obvious from fig. 4.3 (ii). Even at 400 MeV projectile kinetic energy (fig. 4.3 (i)), the difference is rather substantial.

Point P (with appropriate subscript) on curves a and b and c in each of figs. 4.3 (i, ii and iii) denotes the phase where two possible shock configurations meet. Temperatures at these regions as a function of incident lab energy are plotted in fig. 4.4. Once again, we observe the same qualitative natures as in fig. 4.1.

One particular distinction between the plane shock and the oblique shock is that the temperature in the oblique shock is systematically higher than in the plane shock. The reason for this is the following.

For the collision of a single baryon with a heavy ion target, the center of mass frame is effectively the same as

the laboratory frame and there is no reduction in the available kinetic energy. But for a central collision of two equal heavy ions, the lab kinetic energy must be transformed into the center of mass kinetic energy which implies a sizable reduction in the available kinetic energy for thermalization. As seen in the lab frame, the compressed fireball moves with the center of mass velocity, the energy of which is not thermalized. One has also to notice that for an oblique shock, only a part of the target nucleus is compressed (confined by the cone) whereas for a plane shock, the whole system of baryons is compressed.

The range of compression ratios encountered is also very dependent on the equation of state, as expected due to the differences in hardness. For both kinds of shock, the compression ratio for nonrelativistic free gas is 4 (with $\beta = 5/3$). For plane shock, the compression ratio for a relativistic free Fermi gas ranges from 4.15 to 5.51 for the energies considered here whereas the range for the realistic equation of state is from 2.35 to 3.12. The same values are obtained for the oblique shock at the maximum χ.

Due to these high temperatures and associated high specific entropies (calculable from the equation of state) the total heat in the shocked matter is substantial and therefore matter is highly unstable. In order for it to stabilize itself, it must undergo cooling. The appropriate cooling mechanism is determined by the relevant time scales. A discussion of the

cooling mechanism and the hydrodynamic expansion with subsequent fragmentation will be published elsewhere.

Acknowledgement

The authors would like to acknowledge the support of the Department of Energy through contract EY-76-S-05-3992.

References

1. R. L. Bowers, A. M. Gleeson and R. D. Pedigo, Phys. Rev. D12, 3043 (1975); 12, 3056 (1975); J. D. Walecka, Ann. Phys. (N.Y.) 83, 491 (1974).
2. R. L. Bowers, A. M. Gleeson, R. D. Pedigo and J. W. Wheeler, Phys. Rev. D 15, 2125 (1977).
3. R. L. Bowers, A. M. Gleeson and R. D. Pedigo, Nuovo Cimento 41B, 441 (1977).
4. I. D. Novikov and K. S. Thorne, in "Black Holes," Proceedings of 1972 session of Ecole d'été de physique theorique, C. DeWitt and B. S. DeWitt, editors, Gordon and Breach, New York (1973); A. H. Taub, Phys. Rev. 74, 328 (1948); M. H. Johnson and C. F. McKee, Phys. Rev. D3, 848 (1971); A. H. Taub, Ann. Rev. Fluid Mech. 10, 301 (1978).
5. L. D. Landau and E. M. Lifshitz, Fluid Mechanics, Addison-Wesley Publishing Co., Reading, Massachusetts (1959).
6. M. I. Sobel, P. J. Siemens, J. P. Bondorf and H. A. Bethe, Nucl. Phys. A251, 502 (1975).
7. R. Courant and K. O. Friedrichs, Supersonic Flow and Shock Waves, p, 314, Interscience Publishers, Inc., New York (1948).
8. G. F. Chapline, M. H. Johnson, E. Teller and M. S. Weiss, Phys. Rev. D8, 4302 (1973).
9. S. A. Chin, University of Illinois at Urbana-Champaign preprint (1978).

Figure Captions

Fig. 2.1 $\log_{10}$ (pressure) (dynes-cm^{-2}) vs. $\log_{10}$ (number density (cm^{-3}) for the relativistic interacting Fermi fluid. Numbers along curves denote $\log_{10}$T (in °K). For this model, the curve for $\log_{10}$T = 10.0 is representative of all temperature under 10^{10}°K.

Fig. 2.2 $\log_{10}$ (energy density) (gm-cm^{-3}) vs. $\log_{10}$ (number density) (cm^{-3}) for the relativistic interacting Fermi fluid. Numbers along curves denote $\log_{10}$T (°K).

Fig. 2.3 Specific entropy (in units of Boltzmann constant k) vs. $\log_{10}$ (number density) (cm^{-3}) for the relativistic interacting Fermi fluid. Numbers along curves denote $\log_{10}$T (°K).

Fig. 2.4 Specific energy (MeV/baryon) x 10^{-3} vs. $\log_{10}$ (number density) (cm^{-3}) for the relativistic interacting Fermi fluid. Numbers along curves denote $\log_{10}$T (°K).

Fig. 2.5 $\log_{10}$ (pressure) (dynes-cm^{-2}) vs. $\log_{10}$ (number density) (cm^{-3}) for the relativistic free Fermi gas. Numbers along curves denote $\log_{10}$T (°K).

Fig. 2.6 $\log_{10}$ (energy density) (gm-cm^{-3}) vs. $\log_{10}$ (number density) (cm^{-3}) for the relativistic free Fermi gas. Numbers along curves denote $\log_{10}$T (°K).

Fig. 2.7 Specific entropy (in units of Boltzmann constant k) vs. $\log_{10}$ (number density) (cm^{-3}) for the relativistic free Fermi gas. Numbers along curves denote $\log_{10}$T (°K).

Fig. 2.8 $\log_{10}$ (energy density) (gm-cm^{-3}) vs. $\log_{10}$ (number density) (cm^{-3}) for the nonrelativistic Fermi free gas. Numbers along curves denote $\log_{10}$T (°K). As opposed to the relativistic cases, here energy density is the energy less rest mass.

Fig. 2.9 $\log_{10}$ (pressure) (dynes-cm^{-2}) vs. $\log_{10}$ (number density) (cm^{-3}) for the nonrelativistic free Fermi gas. Numbers along curves denote $\log_{10}$T (°K).

Fig. 2.10 $\log_{10}$ (pressure) (dynes-cm^{-2}) vs. $\log_{10}$ (number density) (cm^{-3}) for the nonrelativistic free Boltzmann gas. Numbers along curves denote $\log_{10}$T (°K).

Fig. 3.1 Oblique shock generated by the passage of a supersonic point projectile through semi-infinite slab of fluid. θ is the half-angle of the cone.

Fig. 4.1 Temperature (in MeV) of shocked matter for plane shock vs. laboratory kinetic energy (MeV/baryon).

(a) Relativistic free Fermi gas--temperature generated by a plane compression.

(b) Relativistic free Boltzmann gas--temperature for complete thermalization of initial kinetic energy.

(c) Relativistic interacting Fermi gas--temperature generated by a plane shock compression.

(d) Nonrelativistic free Boltzmann gas--temperature generated by complete thermalization under nonrelativistic kinematics.

(e) Relativistic free Fermi gas--temperature by thermalization of inital kinetic energy assuming that the number density in shocked matter is just twice the initial density.

(f) Nonrelativistic free Fermi gas--temperature generated by a plane shock compression.

Arrow 1 on the abscissa denotes the energy where the center of mass velocity of incoming fluid equals the velocity of sound in the relativistic free Fermi gas and arrow 2 is for the relativistic interacting Fermi gas. Arrow 3 is for a nonrelativistic free Fermi gas.

Fig. 4.2 Schematic diagram for a shock polar. Points P and P' denote the two possible shock configurations corresponding to an angle of deviation χ of incoming velocity. θ is the opening angle for P. P_{ext} denotes where these two possible shocks coincide corresponding to an opening angle θ_{max} and extreme angle of deviation χ_{max}. α is the mach angle.

Fig. 4.3 (i) Shock polar for laboratory kinetic energy of 400 MeV/baryon. Curve a denotes a relativistic noninteracting Fermi fluid. Curve b is for the relativistic interacting Fermi fluid and curve c is for noninteracting nonrelativistic Fermi fluid. Point P on all curves denotes the region where the two shock configurations coincide.

Fig. 4.3 (ii) Shock polar for laboratory kinetic energy of 600 MeV/baryon. Notation is the same as in fig. 4.3 (i). Angles (1) and (2) are the χ_{max} for the relativistic interacting Fermi gas and the relativistic noninteracting Fermi gas, respectively. Angles (3) and (4) are the mach angles for relativistic noninteracting and relativistic interacting Fermi gases, respectively. Angles (5) and (6) are the opening angles (θ_{max}) for relativistic interacting and relativistic noninteracting Fermi gases, respectively.

Fig. 4.3 (iii) Shock polar for laboratory kinetic energy of 800 MeV/baryon. Notation is the same as fig. 4.3 (i).

Fig. 4.4 Temperature (in MeV) generated in an oblique shock (for the region where the two shock configurations coincide in the shock polar) vs. laboratory kinetic energy (in MeV/baryon). Curves a, b and c denote a nonrelativistic noninteracting Boltzmann gas, the relativistic interacting Fermi gas and a relativistic noninteracting Fermi gas, respectively.

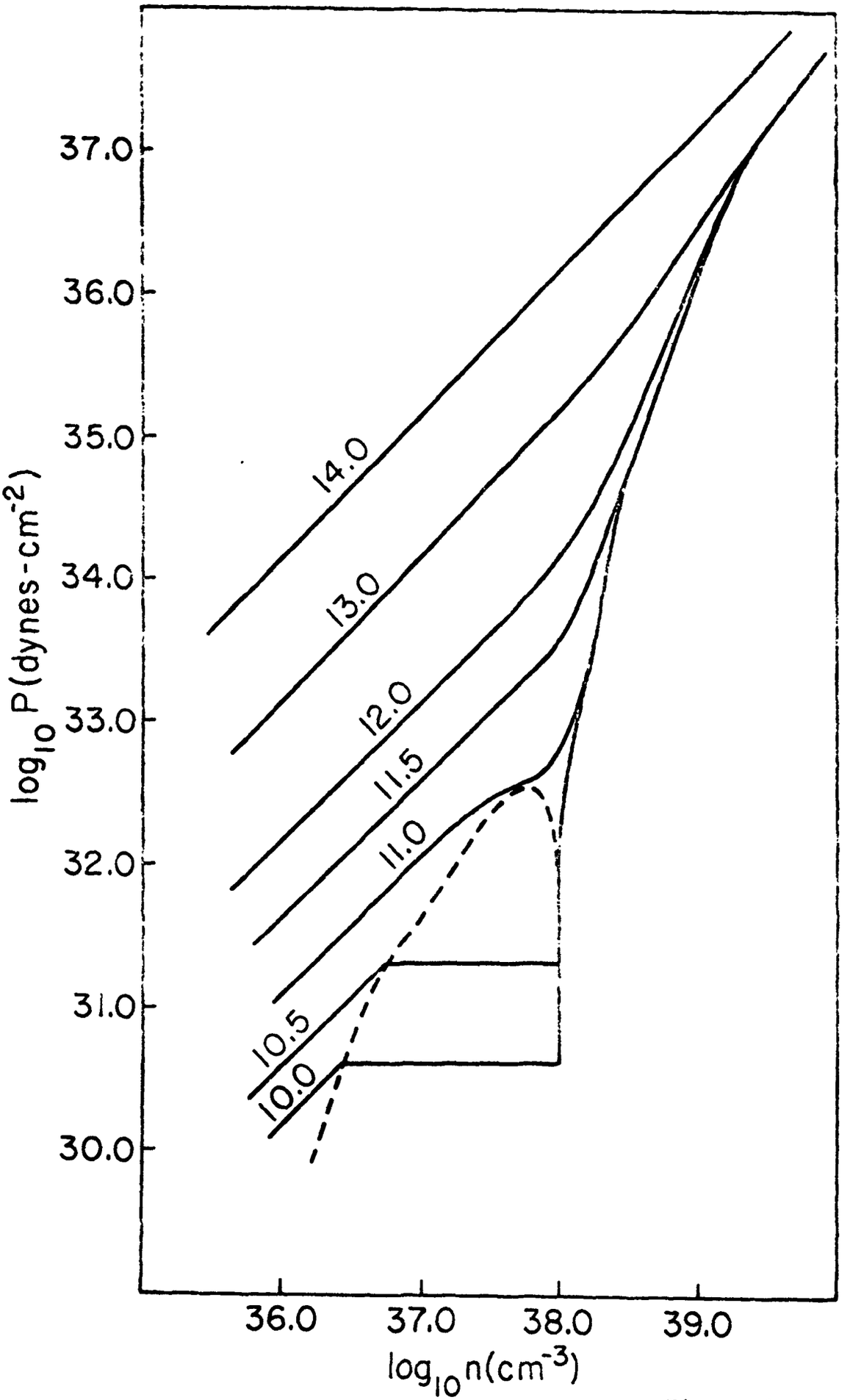
37.0
36.0
35.0
34.0
33.0
32.0
31.0
30.0
$\log_{10} P(\text{dynes-cm}^{-2})$
14.0
13.0
12.0
11.5
11.0
10.5
10.0
36.0
37.0
38.0
39.0
$\log_{10} n(\text{cm}^{-3})$

Figure 2.1

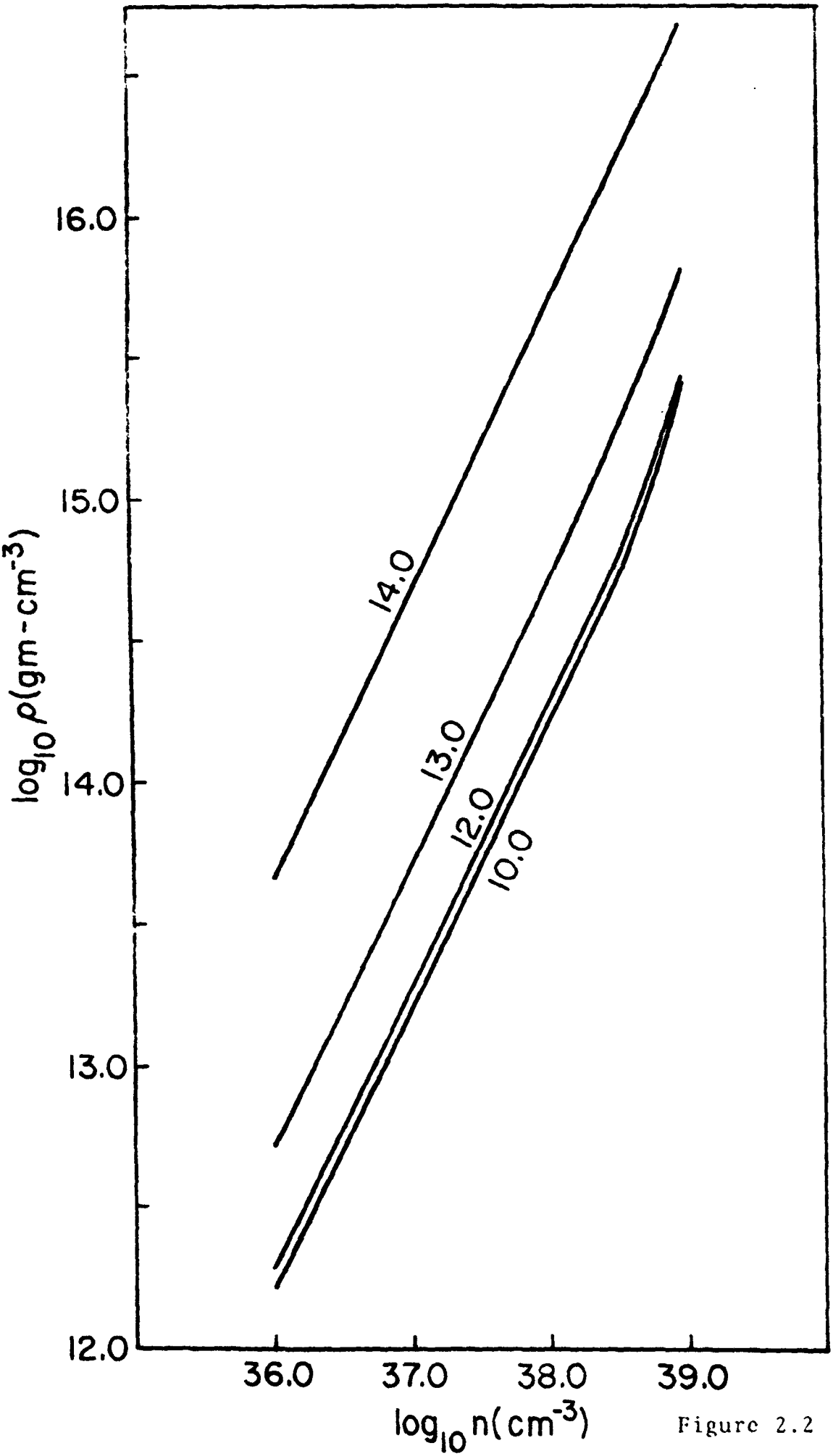
16.0
15.0
14.0
13.0
12.0
$\log_{10}\rho(gm-cm^{-3})$
14.0
13.0
12.0
10.0
36.0
37.0
38.0
39.0
$\log_{10} n(cm^{-3})$

Figure 2.2

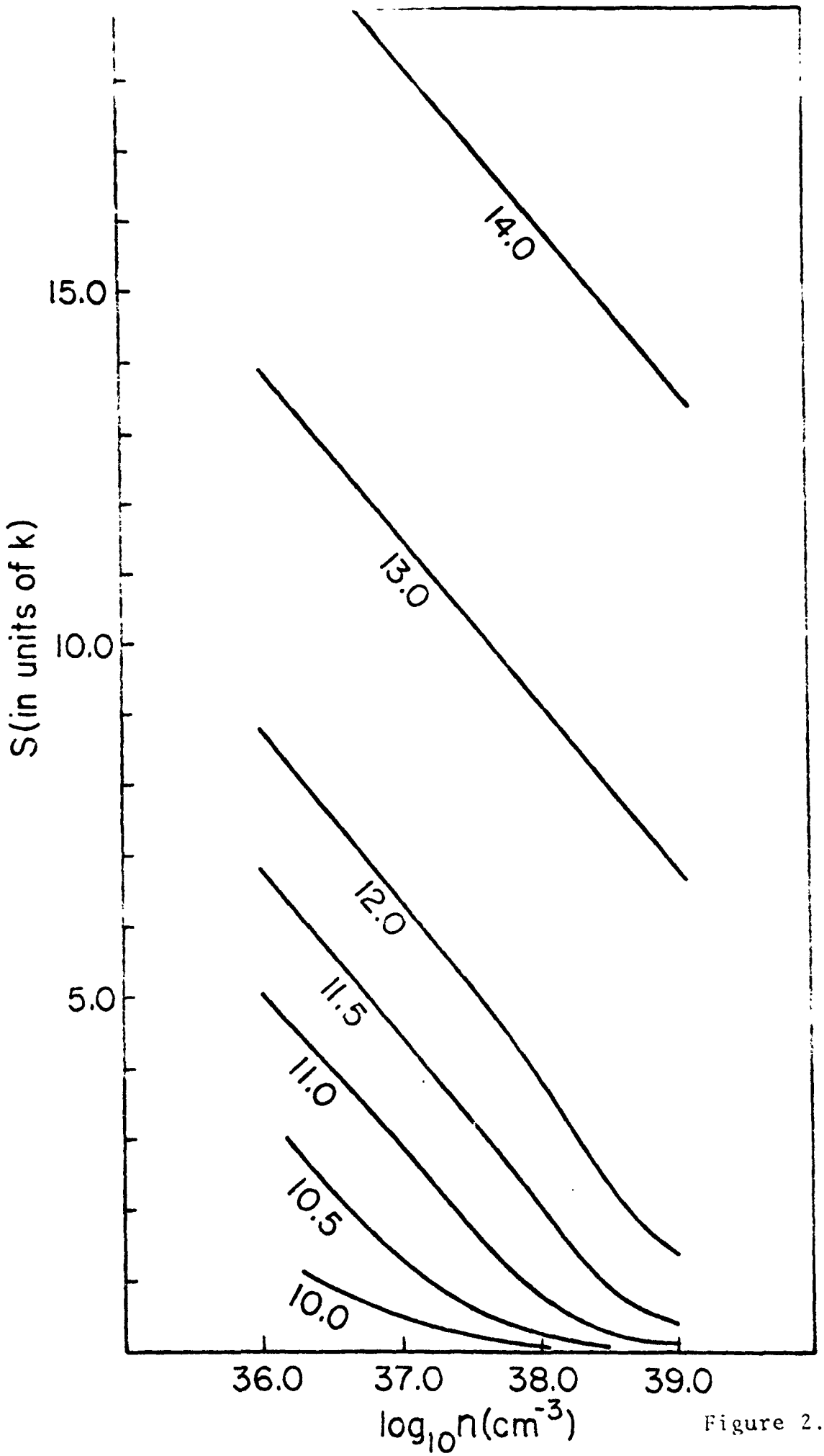
14.0
13.0
12.0
11.5
11.0
10.5
10.0
15.0
10.0
5.0
S(in units of k)
36.0
37.0
38.0
39.0
log10n(cm-3)

Figure 2.3

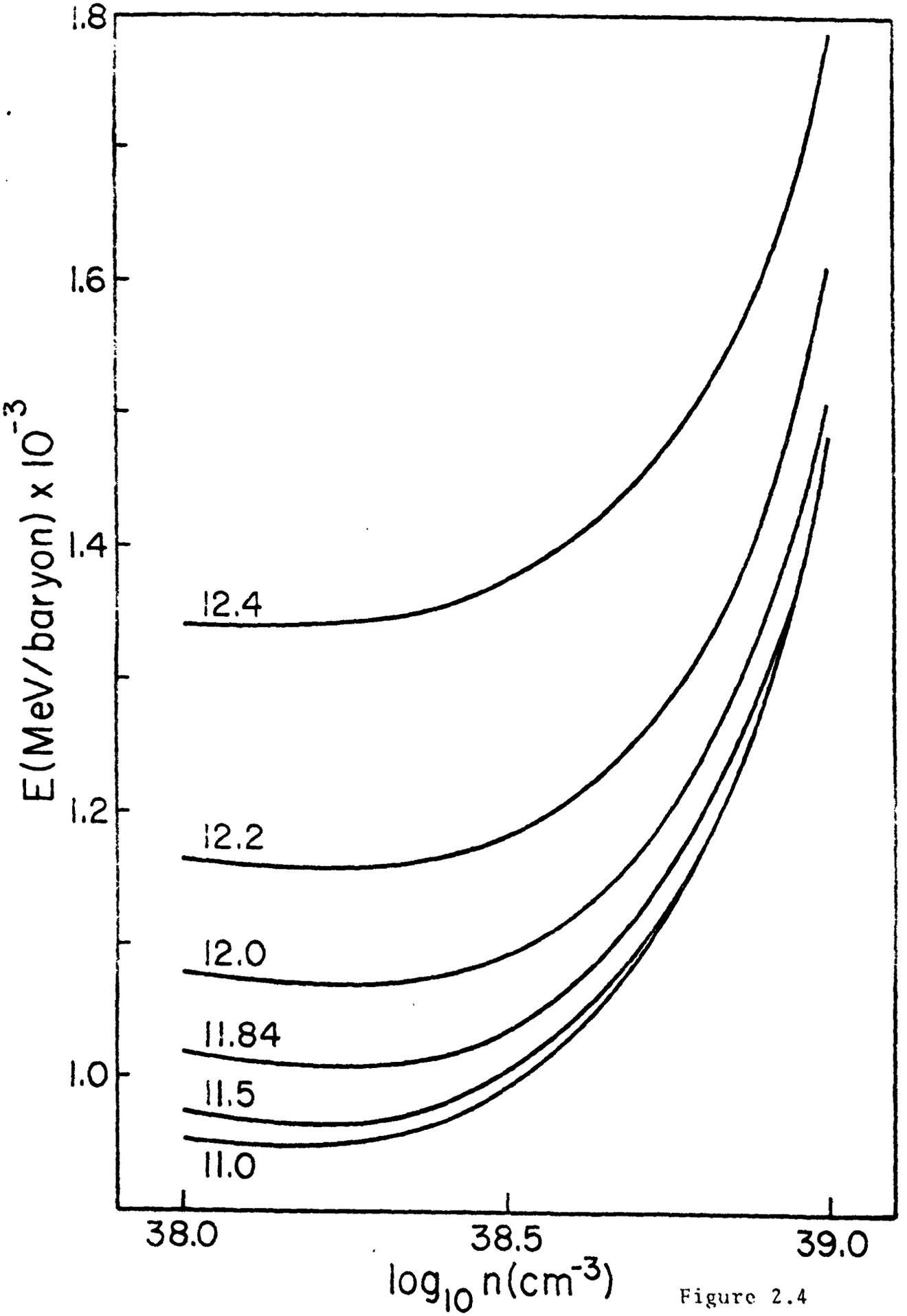
1.8
1.6
1.4
1.2
1.0
E(MeV/baryon) x 10^-3
12.4
12.2
12.0
11.84
11.5
11.0
38.0
38.5
39.0
log10 n(cm^-3)

Figure 2.4

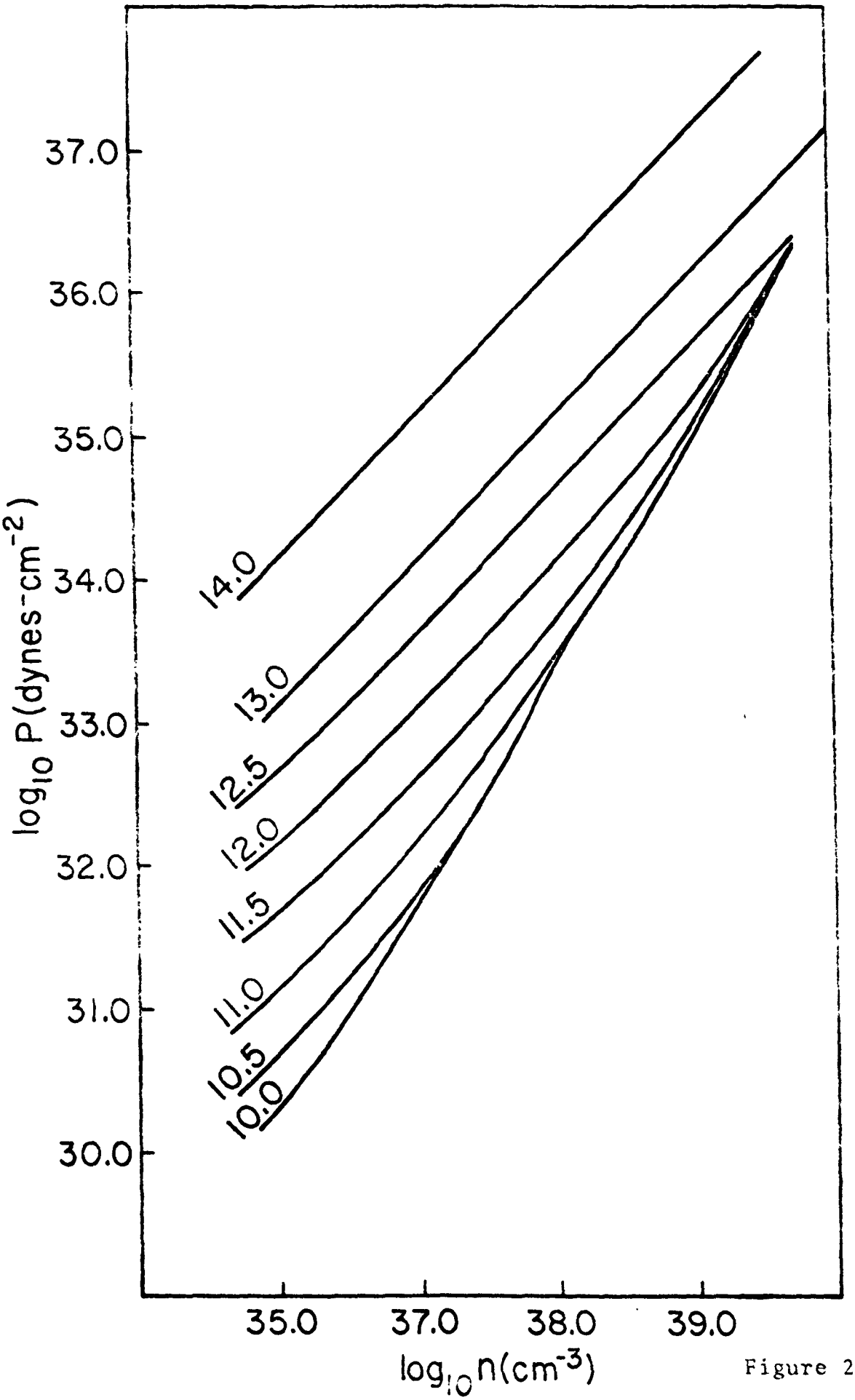
37.0
36.0
35.0
34.0
33.0
32.0
31.0
30.0
log10 P(dynes-cm-2)
14.0
13.0
12.5
12.0
11.5
11.0
10.5
10.0
35.0
37.0
38.0
39.0
log10 n(cm-3)

Figure 2.5

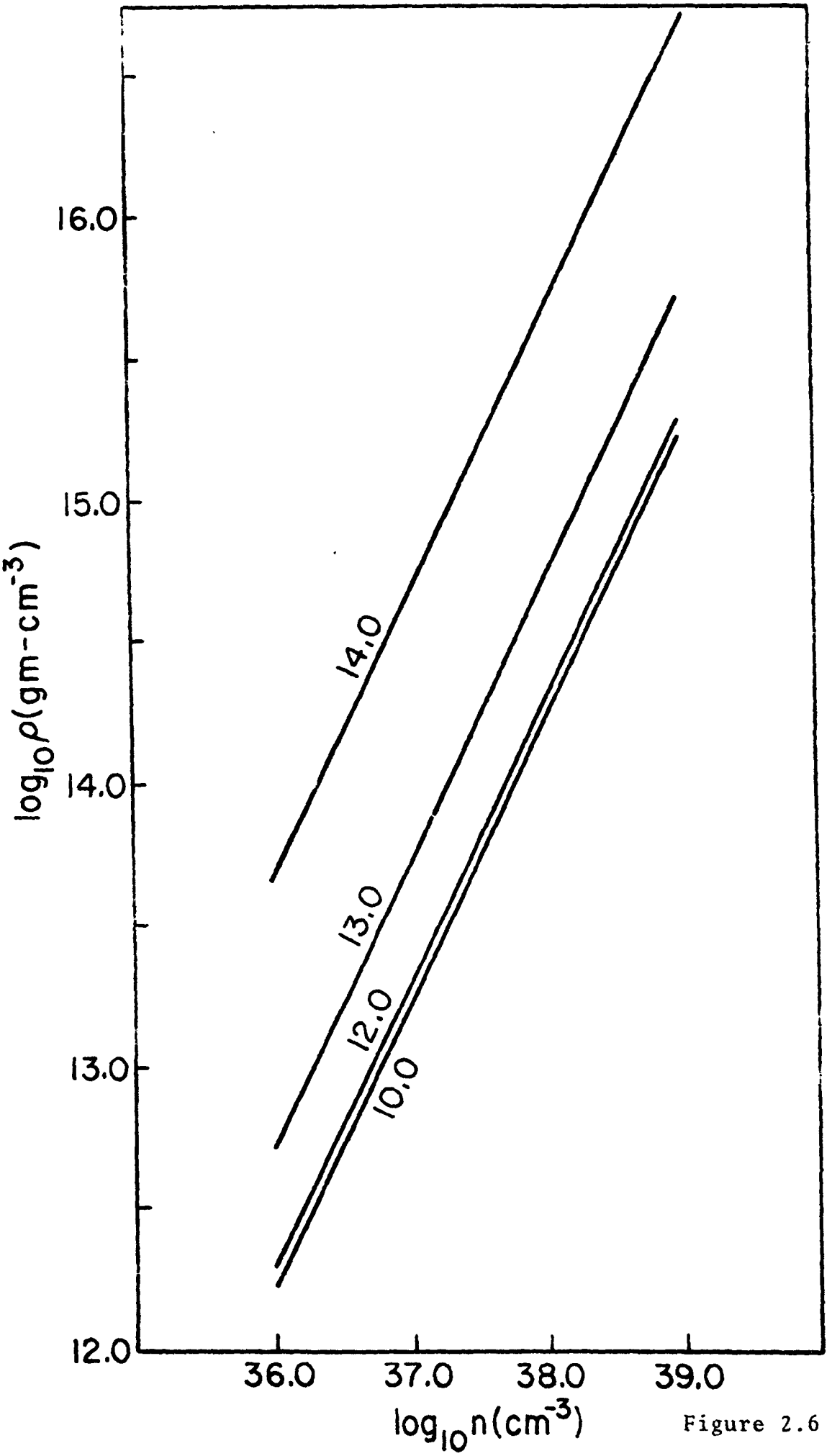
16.0
15.0
14.0
13.0
12.0
$\log_{10}\rho(gm\text{-}cm^{-3})$
14.0
13.0
12.0
10.0
36.0
37.0
38.0
39.0
$\log_{10}n(cm^{-3})$

Figure 2.6

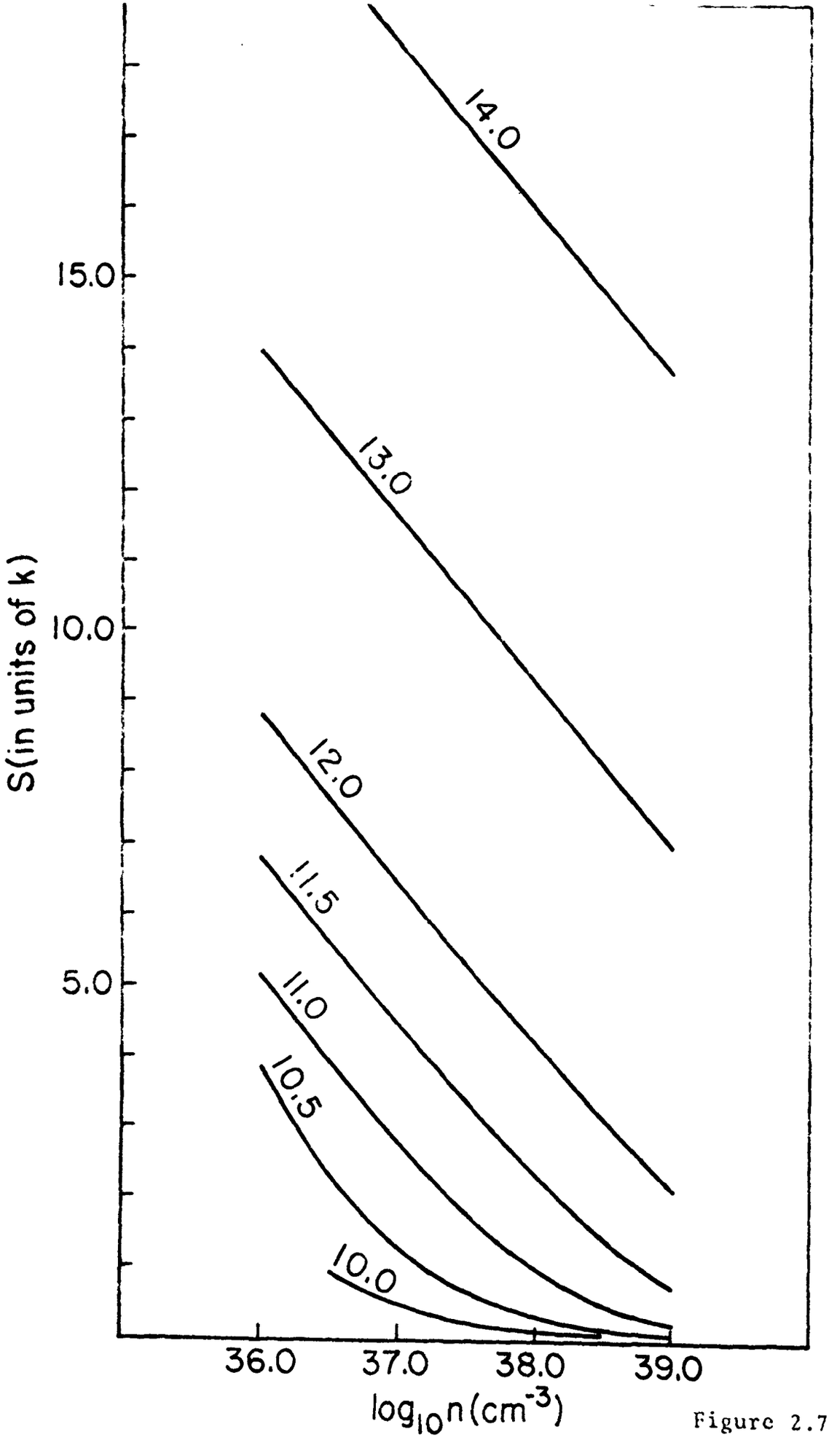
14.0
13.0
12.0
11.5
11.0
10.5
10.0
15.0
10.0
5.0
S(in units of k)
36.0
37.0
38.0
39.0
log10n(cm-3)

Figure 2.7

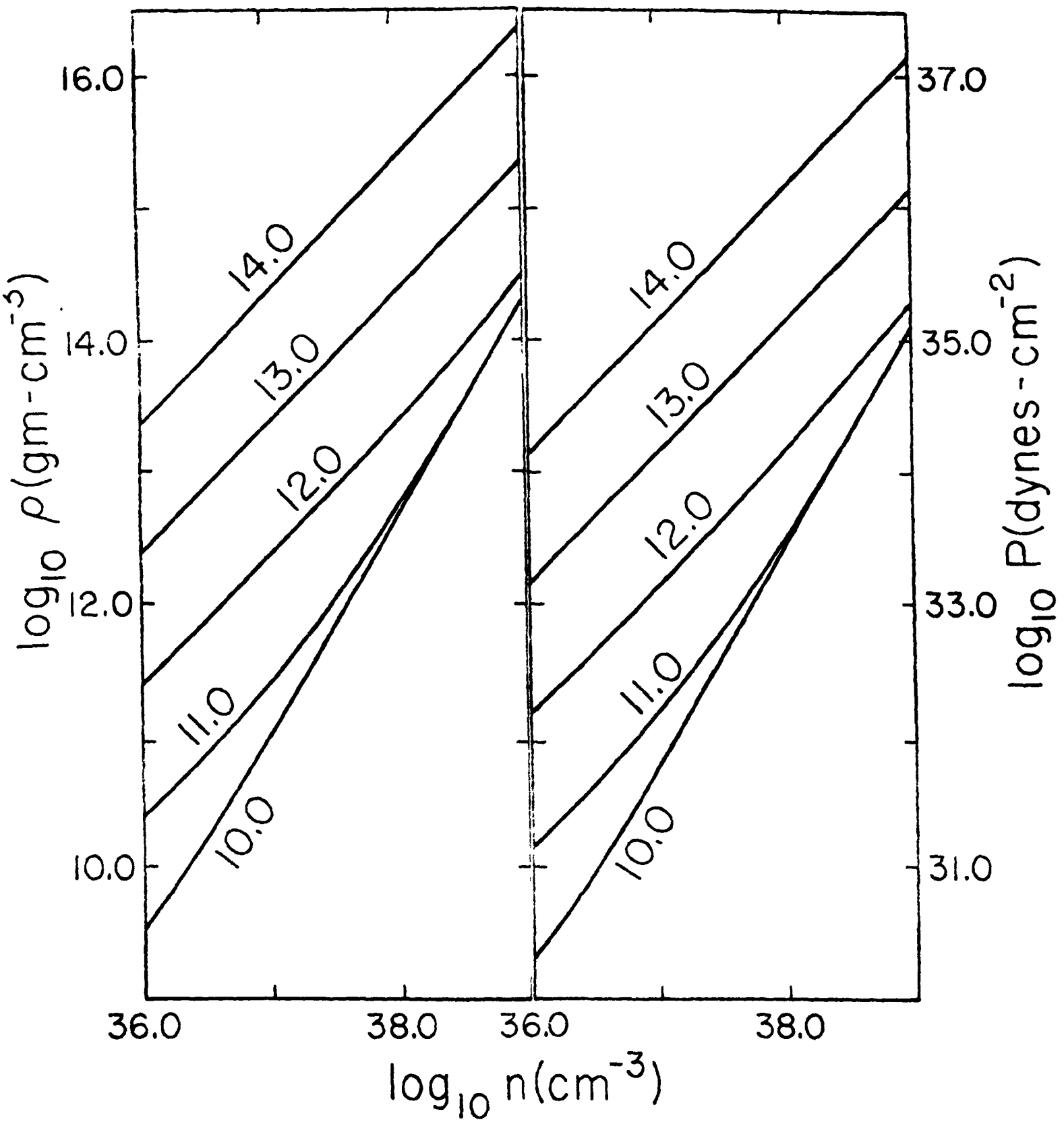

Figure 2.8

Figure 2.9

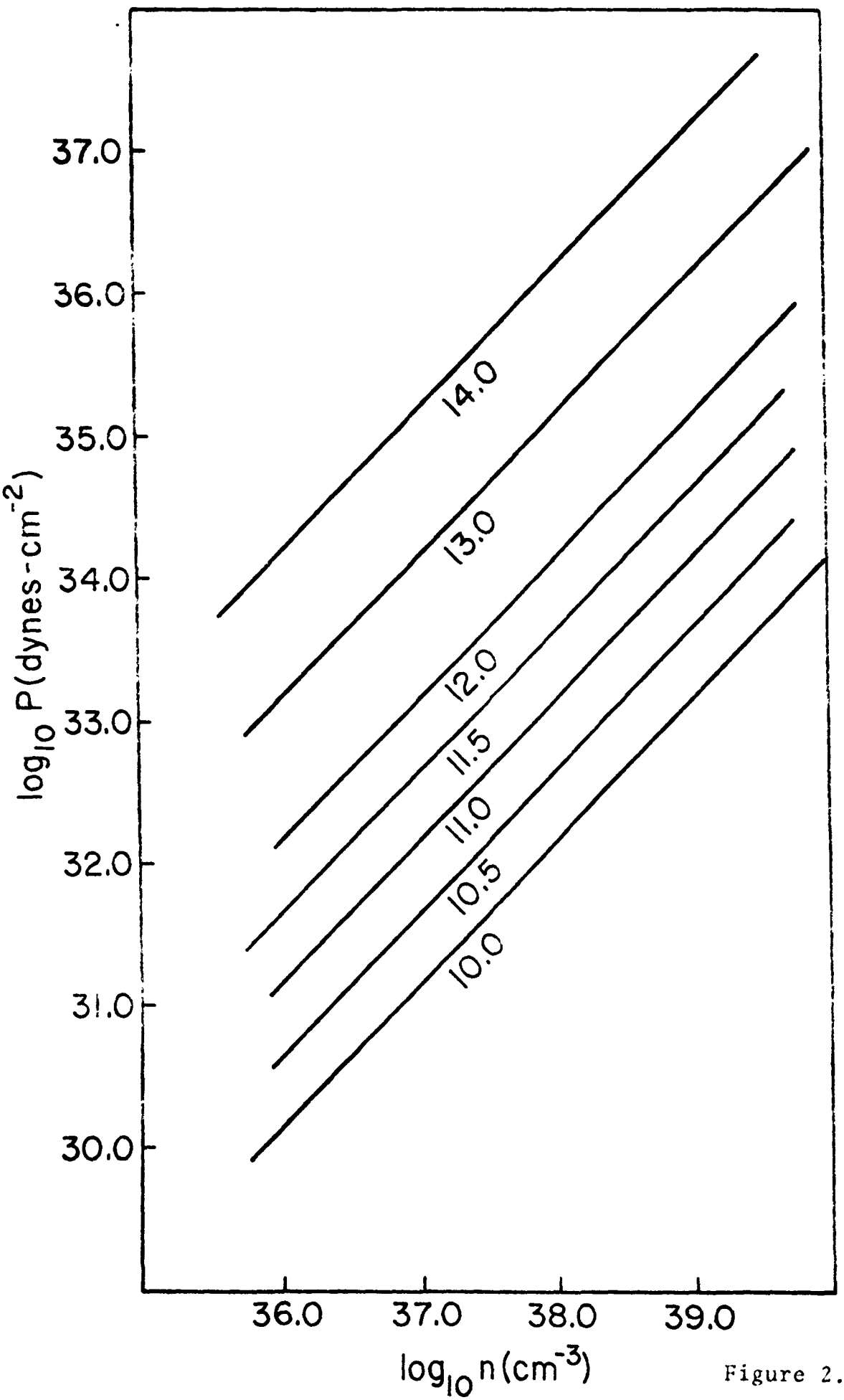
37.0
36.0
35.0
34.0
33.0
32.0
31.0
30.0
$\log_{10} P(\text{dynes-cm}^{-2})$
14.0
13.0
12.0
11.5
11.0
10.5
10.0
36.0
37.0
38.0
39.0
$\log_{10} n(\text{cm}^{-3})$

Figure 2.10

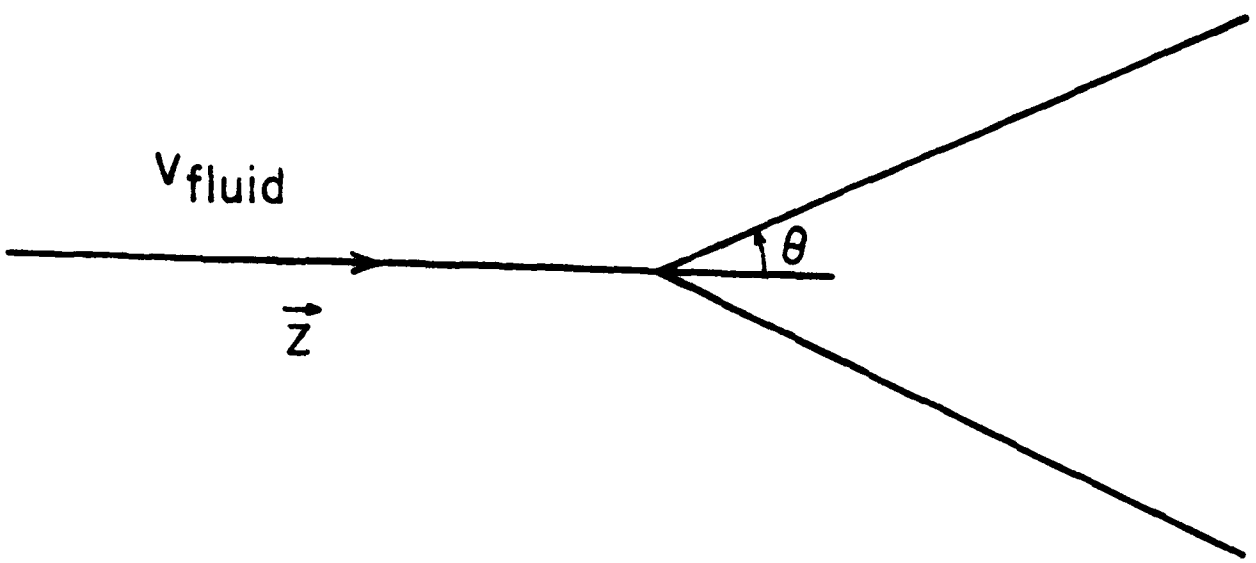

Figure 3.1

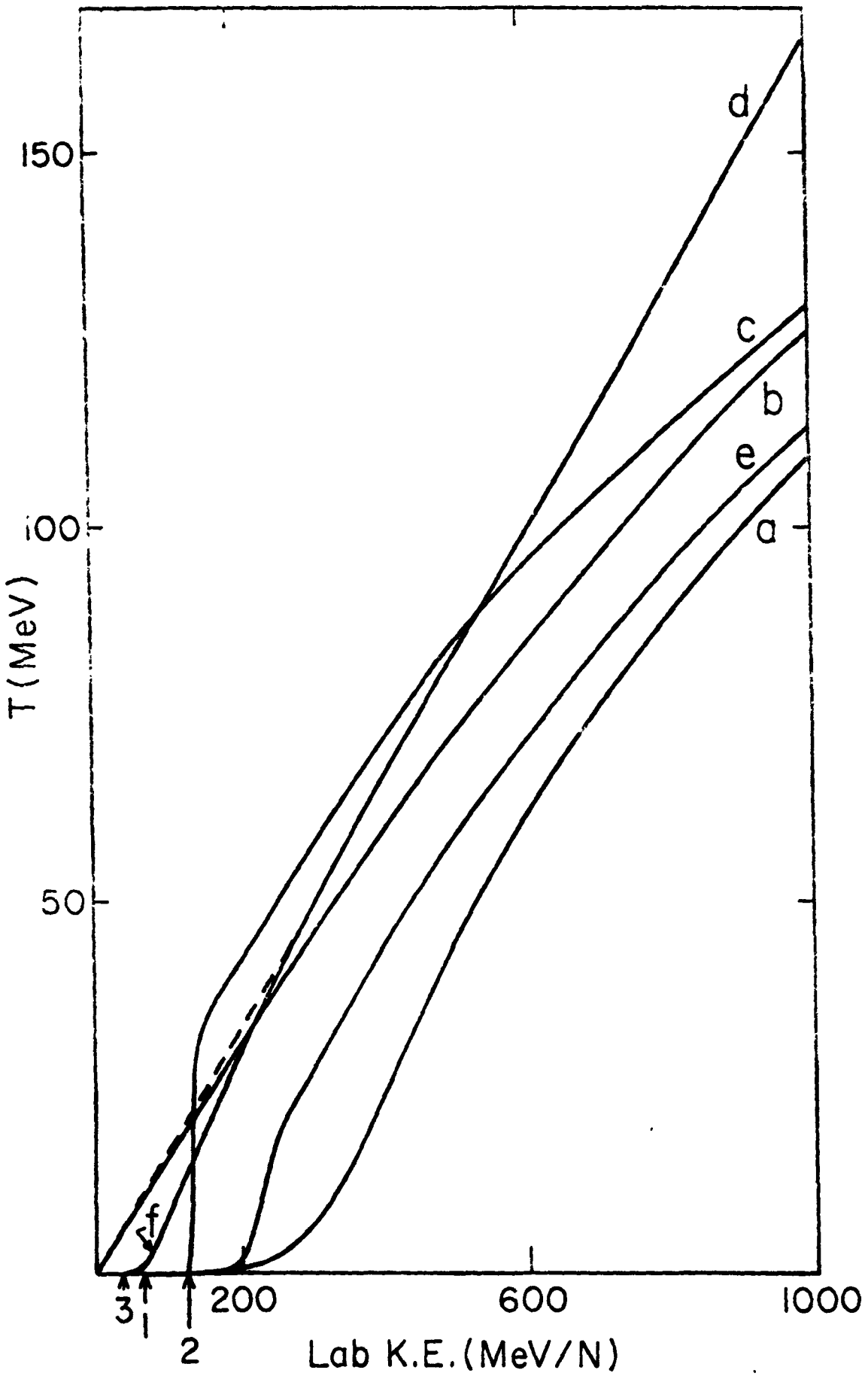

Figure 4.1

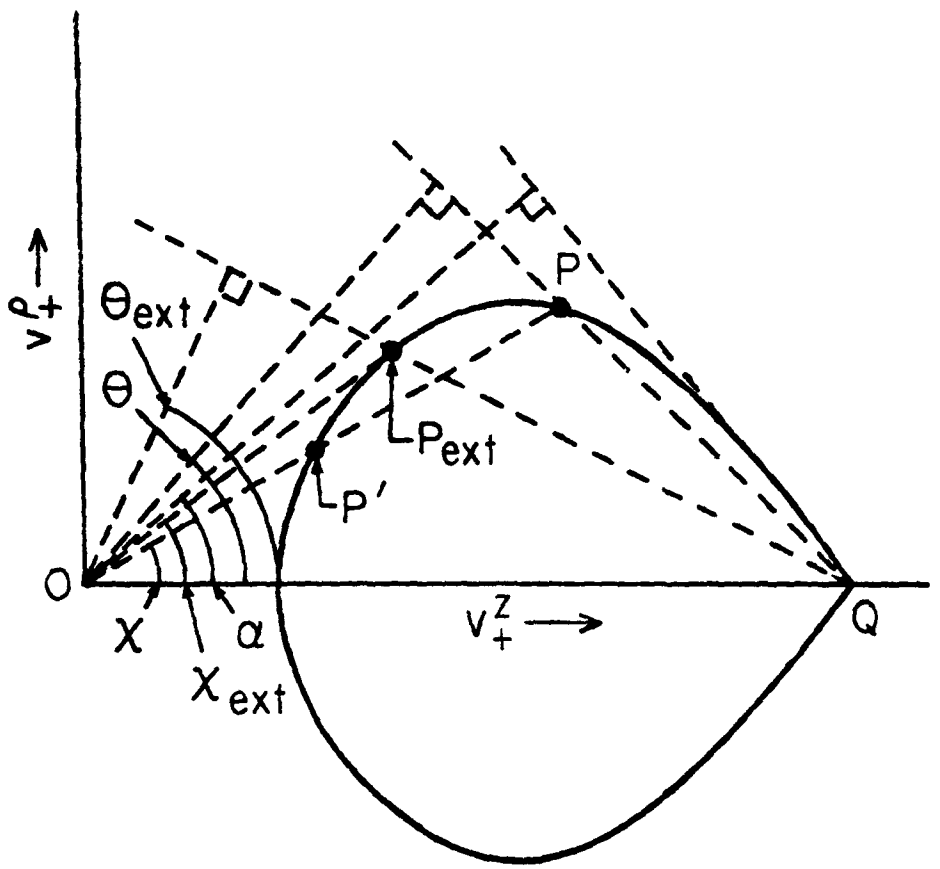

Figure 4.2

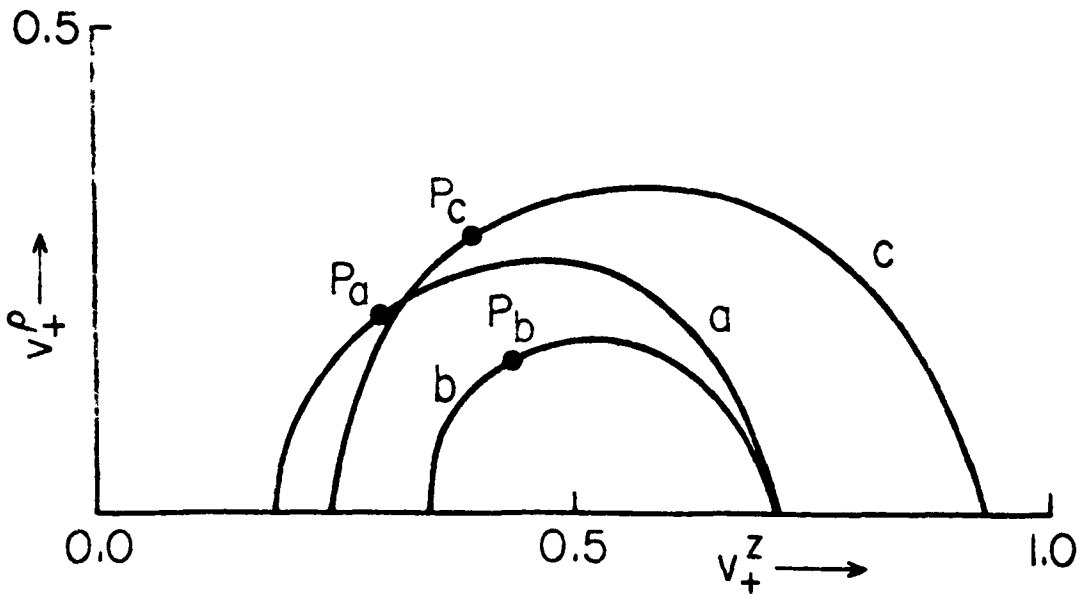

Figure 4.3(i)

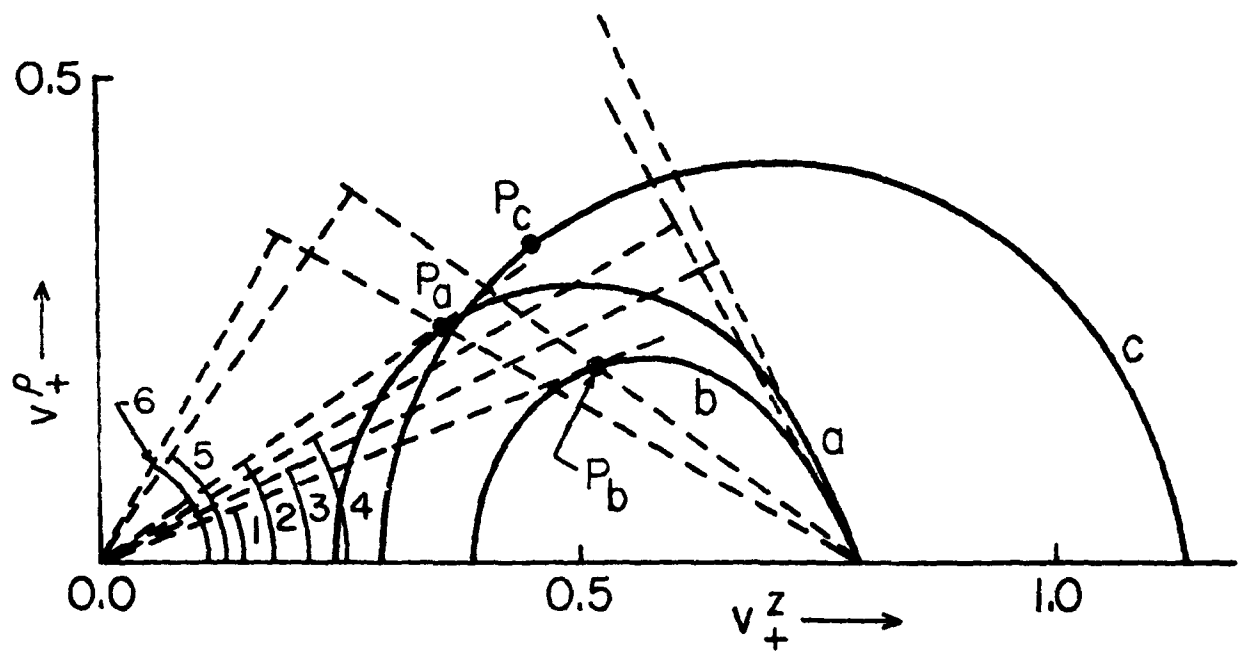

Figure 4.3(ii)

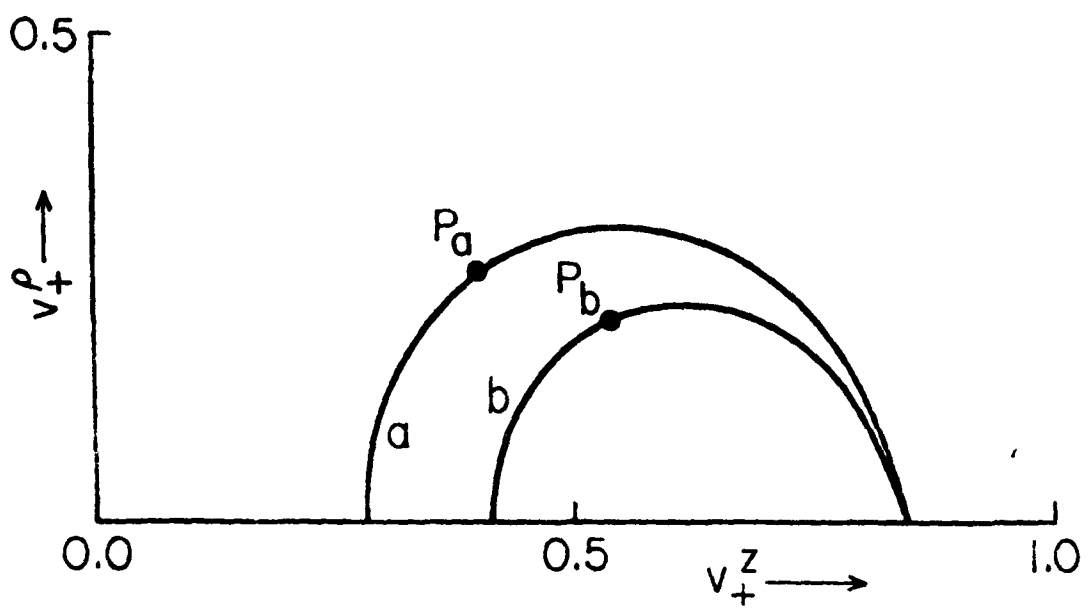

Figure 4.3(iii)

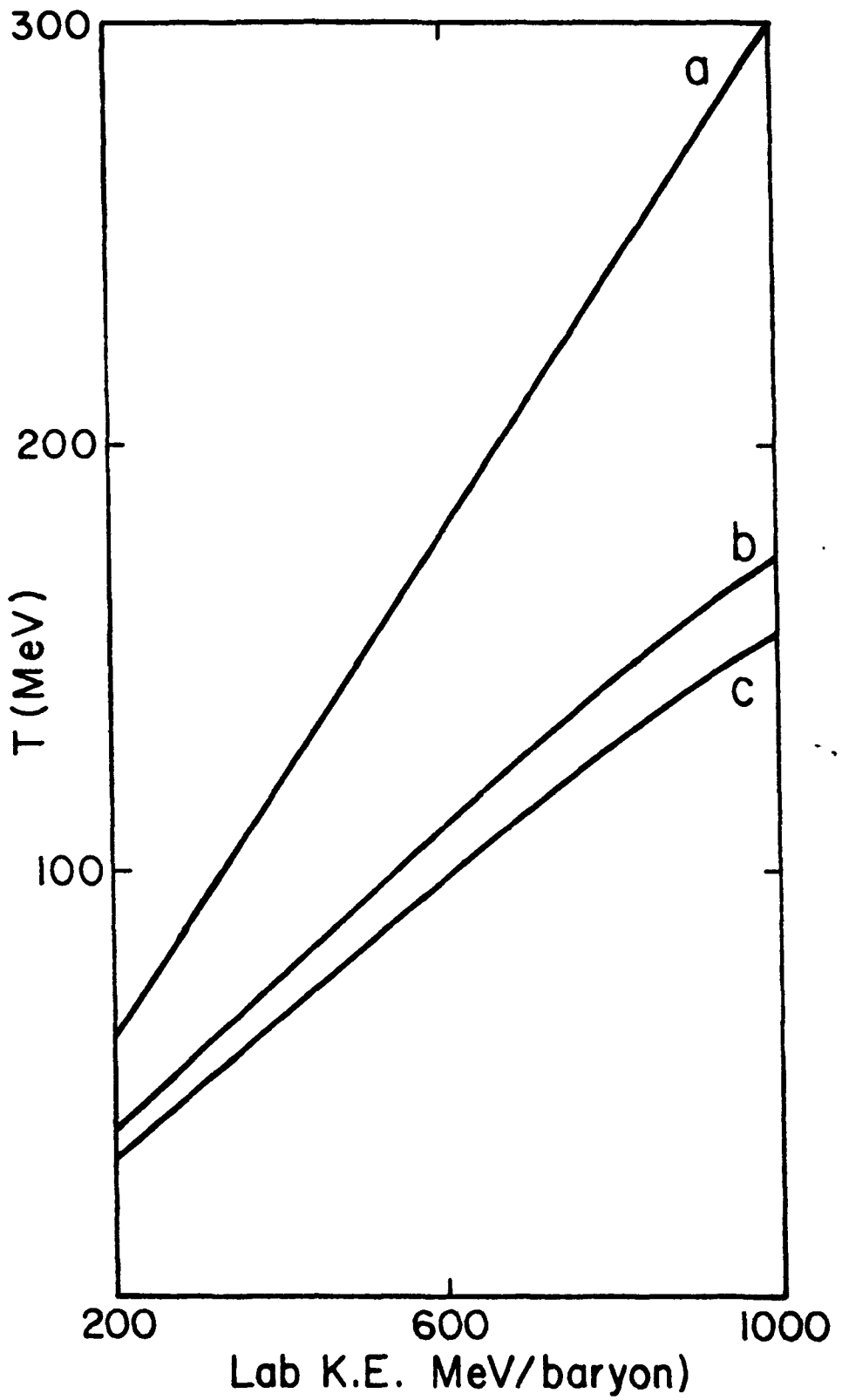

Figure 4.4